

ARTICLE

DOI: 10.1038/s41467-018-07263-1

OPEN

# Resolving orbital pathways for intermolecular electron transfer

Cameron W. Kellett<sup>1</sup>, Wesley B. Swords<sup>2</sup>, Michael D. Turlington<sup>2</sup>,  
Gerald J. Meyer<sup>2</sup> & Curtis P. Berlinguette<sup>1,3,4</sup>

Over 60 years have passed since Taube deduced an orbital-mediated electron transfer mechanism between distinct metal complexes. This concept of an orbital pathway has been thoroughly explored for donor-acceptor pairs bridged by covalently bonded chemical residues, but an analogous pathway has not yet been conclusively demonstrated for formally outer-sphere systems that lack an intervening bridge. In our present study, we experimentally resolve at an atomic level the orbital interactions necessary for electron transfer through an explicit intermolecular bond. This finding was achieved using a homologous series of surface-immobilized ruthenium catalysts that bear different terminal substituents poised for reaction with redox active species in solution. This arrangement enabled the discovery that intermolecular chalcogen...iodide interactions can mediate electron transfer only when these interactions bring the donor and acceptor orbitals into direct contact. This result offers the most direct observation to date of an intermolecular orbital pathway for electron transfer.

<sup>1</sup>Department of Chemistry, 2036 Main Mall, University of British Columbia, Vancouver, BC V6T 1Z1, Canada. <sup>2</sup>Department of Chemistry, University of North Carolina at Chapel Hill, Murray Hall 2202B, Chapel Hill, NC 27599-3290, USA. <sup>3</sup>Department of Chemical and Biological Engineering, 2360 East Mall, University of British Columbia, Vancouver, BC V6T 1Z3, Canada. <sup>4</sup>Stewart Blusson Quantum Matter Institute, 2355 East Mall, University of British Columbia, Vancouver, BC V6T 1Z4, Canada. Correspondence and requests for materials should be addressed to G.J.M. (email: [gjmeyer@email.unc.edu](mailto:gjmeyer@email.unc.edu)) or to C.P.B. (email: [cberling@chem.ubc.ca](mailto:cberling@chem.ubc.ca))

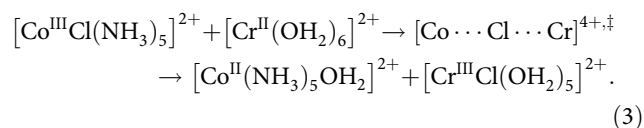
Molecular photoredox catalysis is widely used for a range of applications, such as energy storage<sup>1–3</sup>, CO<sub>2</sub> valorization<sup>4,5</sup>, and organic transformations<sup>6–8</sup>. Typically, light-induced excitation of a photocatalyst creates an energetic electron or hole that enables the transformation of a substrate to a useful product. The discovery and optimization of such catalysts requires the optimization of factors that govern intermolecular electron transfer (IET). In particular, the roles that intermolecular interactions have in mediating electron transfer are very challenging to define. During the last two decades, a body of literature has shown that electrostatic interactions<sup>9,10</sup>, hydrogen bonding<sup>11–13</sup>, and other non-bonding interactions<sup>14–19</sup> can enhance IET rates, but interactions that are too strong may suppress reactivity by lowering the driving force for reaction<sup>20</sup>. This scenario provides the imperative to understand how weak intermolecular interactions can increase IET rates without compromising chemical reactivity.

At a fundamental level, the electron transfer kinetics of molecular donor–acceptor pairs is described by the Marcus equation (equation 1), which is depicted visually in Supplementary Fig. 1. This theory stipulates that the primary factors affecting the rate of electron transfer is the thermodynamic Gibbs free energy change for the reaction ( $\Delta G^\circ_{\text{ET}}$ ) and the reorganization energy ( $\lambda$ ), whereas quantum mechanical effects are accounted for by an electronic coupling factor ( $H_{\text{DA}}$ )<sup>21–23</sup>. While the chemical origins of  $\Delta G^\circ_{\text{ET}}$  and  $\lambda$  are well understood in terms of intuitive chemical principles,  $H_{\text{DA}}$  can only be rigorously defined in terms of the complete wave functions of the non-adiabatic donor–acceptor states before and after electron transfer ( $\Psi_1$  and  $\Psi_2$ , respectively; equation 2)<sup>24</sup>. For formally outer-sphere electron transfer reactions where the electronic coupling is weak,  $H_{\text{DA}}$  can have a significant effect on electron transfer rates<sup>25,26</sup>. Furthermore, early studies on intermolecular self-exchange reactions have suggested that the degree of charge delocalization in conjugated donor or acceptor molecules can have a large impact on the magnitude of  $H_{\text{DA}}$ <sup>27,28</sup>. Nonetheless, for intermolecular systems of even moderate complexity, the structural factors impacting  $H_{\text{DA}}$  are rarely considered. These difficulties stem from the fact that  $H_{\text{DA}}$  is fundamentally a function of the transition state, and therefore challenging to reliably quantify<sup>25,26,29,30</sup>. For donor–acceptor pairs that are covalently bridged, or otherwise bound together on sufficiently long timescales,  $H_{\text{DA}}$  can be inferred from the degree of charge delocalization within the donor–acceptor pairs, which can be measured using vibrational spectroscopy or EPR spectroscopy<sup>31</sup>. Under ideal conditions,  $H_{\text{DA}}$  can also be determined directly using Mulliken-Hush analysis of intervalence charge-transfer excitations in UV-vis-NIR spectroscopy<sup>32–36</sup>. All of these methods require that the donor and acceptor remain in a fixed geometry within the time frame of the experiment, and therefore these analyses are unsuitable for all but a handful of IET reactions that are of practical interest. Computational methods offer somewhat more flexibility with respect to the systems that can be investigated, however challenges remain in balancing reliability for these approaches versus computational cost<sup>30,31,37,38</sup> and thus these methods are not easily accessible to those outside the advanced computational community. Consequently, for experimentalists attempting to design novel molecules, computational methods to predict  $H_{\text{DA}}$  are of limited utility in said design. As such, there is a need in this community to relate  $H_{\text{DA}}$  back to widely understood chemical principles and thereby create intuitive structure–property relationships that can be used to tune this important parameter.

$$k_{\text{Marcus}} = \frac{2\pi}{\hbar} |H_{\text{DA}}|^2 \frac{1}{\sqrt{4\pi\lambda RT}} e^{\left(\frac{-(\lambda + \Delta G^\circ_{\text{ET}})^2}{4RT}\right)}. \quad (1)$$

$$H_{\text{DA}} = \langle \Psi_1 | \hat{H} | \Psi_2 \rangle. \quad (2)$$

The physical meaning of  $H_{\text{DA}}$  is best understood in the context of covalently bonded, inner-sphere donor–acceptor pairs. This understanding stems from Henry Taube's 1953 experiment, where he demonstrated that electron transfer between cobalt(III) chloride and chromium(II) complexes was accompanied by quantitative chloride ligand transfer between the two metal centers (equation 3)<sup>39</sup>. The principal conclusion of this foundational study was that the chloride ligand forms a bridging intermolecular interaction between the two metal centers leading to an increased electron transfer rate compared to complexes that could not form an analogous bridged intermediate. Whereas this intermediate has never been observed, it is generally accepted that it creates an orbital pathway for electron transfer resulting in stronger electronic coupling between the metal centers<sup>29,40</sup>. The effects of these orbital pathways on the rate of electron transfer have been studied extensively for donor–acceptor pairs featuring conjugated covalent bonds or a bridging ligand<sup>40–44</sup>.



Extending this concept of an orbital pathway to non-bonded, formally outer-sphere electron transfer reactions has proven more challenging, though considerable progress has been made in the field of electron transfer in proteins<sup>45–48</sup> and through the use of donor–acceptor pairs rigidly constrained at a fixed distance<sup>49–54</sup>. In these systems, the donor and acceptor are bridged by amino acid residues, by coordinated solvent molecules, or by portions of the rigid backbone itself. In all of these bridged systems, whether covalently bonded or not, electron transfer is understood to be mediated by tunneling pathways, hopping pathways, or super-exchange pathways through the bridging moieties<sup>55,56</sup>.

The common theme among these studies of bridge-mediated electron transfer is that  $H_{\text{DA}}$  is a function of the electronic properties of the bridge as well as the donor and acceptor themselves. In many practically applicable redox catalysis systems; however, the donor and acceptor are not held in a fixed geometry and therefore the bridge is either ill-defined or non-existent. Unfortunately, this means that the knowledge gained from donor–bridge–acceptor systems is of limited utility for the design of molecular redox partners for practical applications. There is consequently a need to understand how the chemical and electronic structure of the isolated donor and acceptor molecules affect electronic coupling in IET processes. Computational studies over the last 10 years have demonstrated that, for bridge-free donor–acceptor pairs, the expression for  $H_{\text{DA}}$  presented in equation 2 can be reasonably simplified to rely only on the frontier molecular orbitals of the donor and acceptor<sup>37,38,57,58</sup>. Following from this description, intermolecular interactions could in principle be leveraged to encourage more interaction between these frontier molecular orbitals and encourage stronger electronic coupling. In practice, while halogen bonding and  $\pi$ -stacking between donor–acceptor pairs have recently been shown to enhance  $H_{\text{DA}}$ <sup>16–19</sup>, the implied orbital pathways for electron transfer have not yet been resolved at the same level of detail possible for covalently bonded systems. This shortcoming stems from the fact that these studies were performed on donor and acceptor molecules in solution, where the interaction of interest is in competition with other secondary interactions (Fig. 1a). Consequently, such studies are typically limited to simple molecules bearing few functional groups in order to limit the number of competing interactions. As a result of this simplicity, modifications intended to perturb the electronic structure of these molecules will invariably change the thermodynamics for IET,

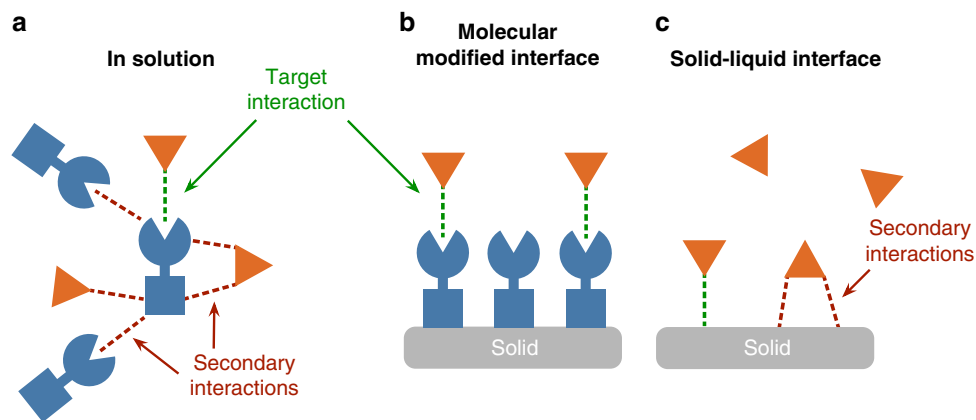


**Fig. 1** Intermolecular interactions in solution and at the interface. A schematic representation of a generic molecule (blue) interacting with a substrate in solution (orange). **a** In solution, many possible interaction sites on the molecule are exposed. **b** When the molecule is anchored to a solid surface, secondary interaction sites are blocked by adjacent molecules. **c** In the absence of a surface-anchored molecular species, the interactions between the substrate and the surface are difficult to conclusively define

complicating any investigation into the effects of electron delocalization. Moreover, any reliance upon dissolved species restricts the accessible time domains for studying IET processes.

We show herein a strategy for overcoming the shortcomings of solution studies by leveraging a solid–liquid interface. The interactions with a solution-phase substrate are poorly resolved on a bare solid surface (Fig. 1c), however, by affixing an appropriately designed molecular species to that surface in a common orientation, specific intermolecular interactions with the substrate can be targeted (Fig. 1b). Constraining the molecules to a surface precludes self-interaction and confines interactions with the soluble substrate to a specific site on the surface-anchored catalyst. We have used this approach previously to demonstrate how specific atoms on organic molecules anchored to TiO<sub>2</sub> can impact IET rates with solution-phase nucleophiles<sup>14,15</sup>. Moreover, the use of photoactive redox catalysts with appropriate excited-state energies relative to the conduction band energy of the metal oxide allows for the generation of strongly oxidizing molecules on ultrafast timescales. This feature of these systems enables the use of pump–probe laser spectroscopy to investigate IET kinetics on timescales that are faster than can be achieved by traditional stop-flow techniques.

We have employed this strategy to demonstrate an explicit atomic orbital pathway for IET mediated by weak intermolecular interactions. To accomplish this, we synthesized two parallel series of cyclometalated ruthenium photoredox catalysts, **X-Ar** (Fig. 2a) and **X-Me** (Fig. 2b), substituted with chalcogen-containing functional groups para- to the ruthenium-carbon bond. With these compounds, we studied the readily accessible oxidation of iodide by the one-electron oxidized catalyst. In this reaction, no covalent bridge exists between the donor and acceptor, and therefore IET must be mediated by transient intermolecular contacts between the iodide donor and the catalyst molecules. It has been previously demonstrated that electron deficient chalcogens can interact with nucleophiles<sup>59–61</sup>, albeit quite weakly in most cases, and previous transient spectroscopic studies have demonstrated that interactions between iodide and sulfur or selenium affect the electron transfer rate constants with iodide<sup>14,62–64</sup>. For the **X-Ar** series, the positive hole, represented by the lowest unoccupied  $\beta$ -spin single electron molecular orbital ( $\beta$ -LUMO), of the oxidized catalyst is delocalized onto the heteroaromatic ring, but not onto the chalcogen atom itself (Fig. 2c). By contrast the positive hole for the **X-Me** series extends significantly onto the heteroatom (Fig. 2c). This difference in hole delocalization means that chalcogen...iodide interactions

encourage direct overlap of the donor orbitals of iodide with the acceptor orbitals of the **X-Me** compounds, while analogous interactions with the **X-Ar** compounds have no effect on the overlap of orbitals relevant to IET. Moreover, because the extent to which the positive hole is delocalized onto the terminal chalcogen atom of the **X-Me** catalysts is a function of heteroatom identity, the degree to which these interactions encourage donor–acceptor orbital overlap varies across this series. As a result, the large rate enhancement of iodide oxidation observed for the **X-Me** series, but not the **X-Ar** series, can be attributed to this orbital pathway through the chalcogen...iodide interactions.

## Results

**Synthesis and preparation of surface-anchored samples.** The ruthenium compounds under investigation were prepared in low to moderate yields from (trimethoxycarbonyl)terpyridine ruthenium trichloride either by direct cyclometalation of the N<sup>^C^A^N</sup> ligand (**X-Ar**, Supplementary Fig. 2), or by transmetalation of an organomercuric chloride precursor (**X-Me**, Supplementary Fig. 3). NMR spectra of the final compounds and synthetic intermediates are presented in Supplementary Note 1. Solution phase optical and electronic characterization was carried out on the methyl ester complexes as tetrafluoroborate salts. To prepare surface-anchored samples for photophysical experiments, the compounds were saponified as described in the Supplementary Methods and reacted with mesoporous semiconductor films from saturated ethanol solutions. Depending on the experiment, mesoporous thin films made from TiO<sub>2</sub> nanoparticles, SnO<sub>2</sub>–TiO<sub>2</sub> core-shell nanoparticles, or indium-doped SnO<sub>2</sub> nanoparticles (nano-ITO) were employed as indicated. All thin films were prepared on glass substrates coated with fluorine-doped tin oxide. The oxygen containing analogue of the **X-Ar** series, **O-Ar**, decomposed rapidly following saponification and was therefore not evaluated.

**Optical and redox properties.** The absorption maxima,  $\lambda_{\text{max}}$ , for each of the major bands for the **X-Me** and **X-Ar** series were determined by UV-vis spectroscopy and varied by less than 10 nm across all compounds when measured in acetonitrile (MeCN) solution (Supplementary Fig. 4a, Table 1). Upon saponification and adhesion to TiO<sub>2</sub>, the lowest energy metal-to-ligand charge-transfer (MLCT) transition of each catalyst was hypsochromically shifted  $\sim 20$  nm relative to the methyl esters, with no other significant changes (Supplementary Fig. 4b, Table 1). The Ru<sup>III/II</sup>

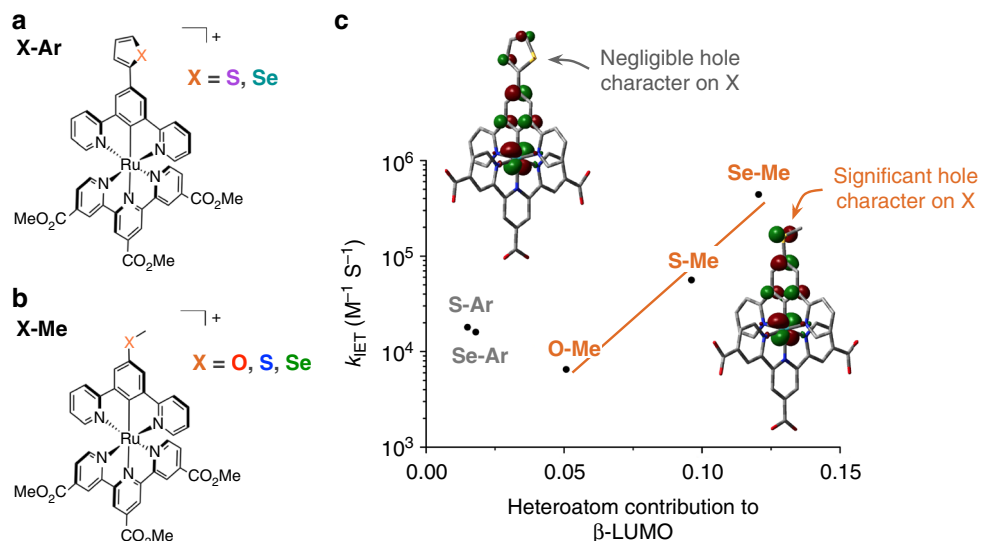


**Fig. 2** Ruthenium complexes to control  $\beta$ -LUMO delocalization. **a, b** Chemical structures of the **X-Ar a** and **X-Me b** compounds under investigation. The methyl ester groups are converted to acids to enable binding to titania. **c** Plot of the second-order IET rate constant ( $k_{\text{IET}}$ ) for the indicated compounds versus the heteroatom contribution to the  $\beta$ -LUMO ( $c_{\text{A,X}}$ ), overlaid with representative visualizations of the  $\beta$ -LUMO of **X-Ar** (left) and **X-Me** (right) plotted at an iso-value of 0.05

**Table 1** Optical and redox properties of ruthenium complexes in solution and immobilized on mesoporous metal oxide ( $\text{MO}_x$ ) thin films

Compound	$\lambda_{\text{max, MeCN}}$ (nm) <sup>a</sup>	$\epsilon_{\text{MeCN}}$ ( $\times 10^4 \text{ M}^{-1} \text{ cm}^{-1}$ ) <sup>a</sup>	$E_{1/2, \text{MeCN}}$ ( $\text{Ru}^{\text{III/II}}$ ) (V) <sup>b</sup>	$\lambda_{\text{max, MO}_x}$ (nm) <sup>c</sup>	$E_{1/2, \text{MO}_x}$ ( $\text{Ru}^{\text{III/II}}$ ) (V) <sup>d</sup>
<b>O-Me</b>	589	1.04	0.78	570	0.73
<b>S-Me</b>	583	1.09	0.84	566	0.80
<b>Se-Me</b>	583	1.12	0.86	564	0.82
<b>S-Ar</b>	582	1.09	0.88	562	0.85
<b>Se-Ar</b>	582	1.19	0.88	561	0.84

<sup>a</sup>Measurements are reported in V vs NHE and were collected in acetonitrile solution

<sup>b</sup>Collected in 0.1 M  $(\text{NBu}_4)\text{BF}_4$  acetonitrile solution and referenced to an external ferrocene/ferrocenium standard (0.630 V vs NHE)<sup>75</sup>

<sup>c</sup>Saponified catalysts on  $\text{TiO}_2$  thin films

<sup>d</sup>Measurements of the saponified catalysts are reported in NHE and were collected on nano-ITO thin films immersed in 0.5 M  $\text{NaClO}_4$  acetonitrile solution and  $E_{1/2}$  values determined by deconvolution of the resulting spectra into oxidized and reduced components (Supplementary Fig. 5b)

redox couples for the compounds were determined by cyclic voltammetry in acetonitrile solution (Supplementary Fig. 4c, Table 1). All compounds displayed quasi-reversible redox couples with 75–80 mV peak separations. All  $\text{Ru}^{\text{III/II}}$  couples fall within the narrow electrochemical window of 0.84–0.88 V vs NHE with the exception of **O-Me**, which displayed a redox couple cathodically shifted ~60 mV.

The optical and redox properties of the saponified catalysts anchored to metal oxide films were investigated through spectroelectrochemistry on nano-ITO (Supplementary Fig. 5, Table 1). The  $\text{Ru}^{\text{III/II}}$  couples were cathodically shifted ~40 mV versus the methyl esters in solution, though they remained in a relatively narrow window of 0.80–0.85 V vs NHE, except for **O-Me** which was still ~60 mV more cathodic than **S-Me**. Upon oxidation by one electron, the absorbance spectra recorded for each of the oxidized complexes featured a prominent new low-energy absorption band centered between 700 and 850 nm coupled with a bleach of the  $\text{Ru}^{\text{II}}$  MLCT band, consistent with the formation of a  $\text{Ru}^{\text{III}}$  complex. Sharp isosbestic points were observed for each of the compounds between 650 and 700 nm, indicating clean conversion of the  $\text{Ru}^{\text{II}}$  to the  $\text{Ru}^{\text{III}}$  complexes with no side reactions. Exchange of oxygen to sulfur and selenium in the **X-Me** catalysts resulted in an increasing bathochromic shift of the new absorption band by 95 nm ( $1690 \text{ cm}^{-1}$ ) and 45 nm

( $810 \text{ cm}^{-1}$ ), respectively. In contrast the exchange of selenium for sulfur in **X-Ar** results in a much more modest 25 nm ( $240 \text{ cm}^{-1}$ ) bathochromic shift.

**Interfacial chemistry.** Electron-transfer kinetics were studied at the interface of mesoporous  $\text{TiO}_2$  thin films functionalized with **X-Me** or **X-Ar** submerged in solutions containing either 0.5 M  $\text{NaClO}_4/\text{MeCN}$  or 0.5 M  $\text{NaI}/\text{MeCN}$ . The critical electron transfer reactions that occur at photocatalyst-functionalized  $\text{TiO}_2$  surfaces are depicted in Fig. 3a. Following laser excitation of the films at 532 nm, electrons are injected from the excited photo-redox catalyst into the  $\text{TiO}_2$  conduction band. This process results in the appearance of an optical signal consistent with oxidized **X-Me**<sup>•+</sup> or **X-Ar**<sup>•+</sup> (Supplementary Fig. 6). In the redox inert  $\text{NaClO}_4$  electrolyte, the injected electrons and oxidized catalysts on the surface recombine in a process called back-electron transfer (BET). In the presence of  $\text{NaI}$  electrolyte, the photo-oxidized catalyst instead oxidizes iodide through an IET process. To accurately resolve IET kinetics, it is necessary that the rate constant for IET ( $k_{\text{IET}}$ ) be much greater than that for BET ( $k_{\text{BET}}$ ). On pure  $\text{TiO}_2$  thin films, the BET rates were found to be too similar to the IET rates to enable accurate determination of the true second-order  $k_{\text{IET}}$ , and  $\text{TiO}_2$  was therefore not a good

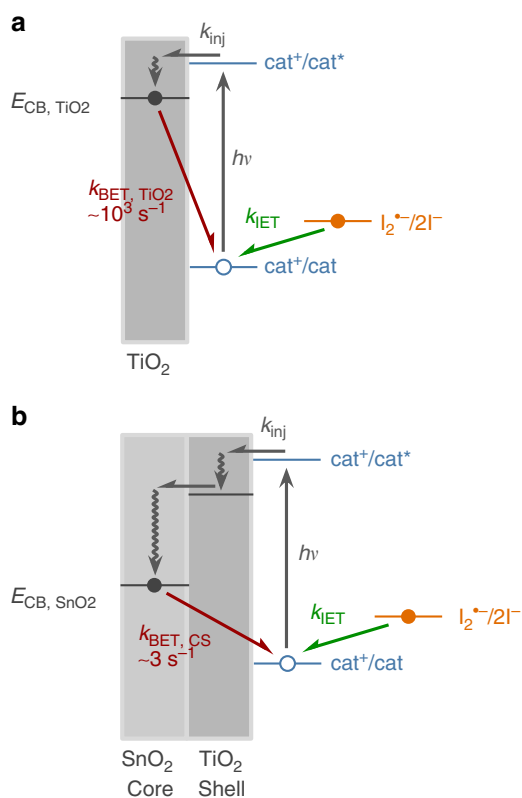


**Fig. 3** Electron transfer reactions at photoredox functionalized metal oxide interfaces. A schematic depicting the major electron transfer reactions that occur at functionalized  $\text{TiO}_2$  (**a**) or  $\text{SnO}_2$ - $\text{TiO}_2$  core-shell (**b**) interfaces: excitation of the catalyst by a photon ( $h\nu$ ), electron injection into the semiconductor ( $k_{\text{inj}}$ ), back-electron transfer ( $k_{\text{BET}}$ ), and intermolecular electron transfer ( $k_{\text{IET}}$ ). The energy levels of the catalyst redox potentials in the ground and excited states ( $\text{cat}^+/\text{cat}$  and  $\text{cat}^+/\text{cat}^*$ , respectively), the diiodide redox potential ( $\text{I}_2^{\bullet-}/2\text{I}^-$ ), and the conduction bands of  $\text{TiO}_2$  and  $\text{SnO}_2$  ( $E_{\text{CB, TiO}_2}$  and  $E_{\text{CB, SnO}_2}$ , respectively) are depicted on an approximate relative energy scale

**Table 2** Electron transfer kinetics and  $\beta$ -LUMO partition

Compound	$k_{\text{BET, TiO}_2}$ ( $\times 10^4$ $\text{s}^{-1}$ ) <sup>a</sup>	$k_{\text{BET, CS}}$ ( $\text{s}^{-1}$ ) <sup>b,c</sup>	$k_{\text{IET}}$ ( $\times 10^4$ $\text{M}^{-1} \text{s}^{-1}$ ) <sup>b</sup>	Heteroatom contribution to $\beta$ -LUMO, $c_{\text{A}, \text{X}}$ <sup>d</sup>
<b>O-Me</b>	4.8	1.1	0.65	0.051
<b>S-Me</b>	2.2	2.7	5.6	0.096
<b>Se-Me</b>	0.44	1.9	44	0.121
<b>S-Ar</b>	0.080	3.0	1.8	0.015
<b>Se-Ar</b>	0.092	3.4	1.6	0.018

<sup>a</sup>Saponified catalysts adsorbed to  $\text{TiO}_2$  thin films

<sup>b</sup>Saponified catalysts anchored to  $\text{SnO}_2$ - $\text{TiO}_2$  core-shell thin films

<sup>c</sup>Modeled with the KWW function,  $\beta$  fixed to 0.3

<sup>d</sup>Calculated from DFT models using a Hirshfeld partition of the MO density and expressed as a fraction of unity

substrate to fully analyze the iodide oxidation kinetics (Supplementary Fig. 7a, Table 2).

$\text{SnO}_2$ - $\text{TiO}_2$  core-shell mesoporous thin films have been shown to drastically prolong BET reaction lifetimes<sup>65</sup>. In these films, an excited electron injected into the  $\text{TiO}_2$  shell quickly migrates into the more positive conduction band of the  $\text{SnO}_2$  core (Fig. 3b). From there, in order to undergo BET, the electron must tunnel through the shell to recombine with the oxidized catalyst on the surface. When **X-Me** and **X-Ar** were anchored to these core-shell

thin films,  $k_{\text{BET}}$  was found to decrease by almost two orders of magnitude compared to the  $\text{TiO}_2$  thin film samples (Supplementary Fig. 7b), and was the same within experimental error for all catalyst compounds (Supplementary Fig. 8, Table 2). This allowed IET rate constants to be determined. The IET rates were studied in an analogous method to BET, but in the presence of increasing concentrations of iodide (Supplementary Fig. 9). From this data, we extracted the true second-order  $k_{\text{IET}}$  values (Supplementary Fig. 10, Table 2). In the **X-Me** series, an order of magnitude increase in  $k_{\text{IET}}$  was observed on exchanging S for O, and again when exchanging Se for S (Supplementary Fig. 10a). By contrast, in the **X-Ar** series, no significant change in  $k_{\text{IET}}$  was observed between **S-Ar** and **Se-Ar** (Supplementary Fig. 10b). In previous studies, catalyst structure has also been shown to have an effect on the rate of charge recombination between injected electrons and the oxidized form of the electrolyte<sup>62,63</sup>; however, the rate constant for this reaction was found to be the same for all compounds currently under investigation (Supplementary Fig. 11).

## Discussion

The compounds under investigation were designed to ensure optimal electronic and geometric properties for the systematic study of both intermolecular interactions and electron transfer (Fig. 2a, b). The highest occupied molecular orbital (HOMO) energy of the compounds is primarily a product of ruthenium centered molecular orbitals. Cyclometalation of the ruthenium shifts the HOMO higher in energy relative to the far more extensively studied ruthenium complexes bearing neutral ligands, but remains sufficiently positive to oxidize iodide<sup>66,67</sup>. The tricarboxyterpyridine ligand was chosen to ensure that the lowest unoccupied molecular orbital (LUMO) energy of the reduced  $\text{Ru}^{\text{II}}$  catalysts were appropriately positioned to inject electrons into  $\text{TiO}_2$  and to anchor the catalysts to the metal oxide substrates<sup>67</sup>. Previous studies have shown that incorporation of chalcogen atoms in positions with access to the metal oxide surface can encourage side reactions between the electrolyte and the semiconductor<sup>62-64</sup>, and therefore **X-Me** and **X-Ar** were substituted para- to the ruthenium center on the central ring to direct the chalcogen atoms away from the surface. The  $\text{N}^{\wedge}\text{C}^{\wedge}\text{N}$  cyclometalating motif was chosen such that, upon oxidation, the resulting positive hole will be delocalized to encompass the central ring and its substituents, ensuring that this hole will be exposed to the solution.

The HOMO and LUMO are important orbitals in chemical transformations like IET. As a result, the delocalization of these frontier orbitals within a molecular structure strongly impacts the properties and reactivity of that molecule. Upon substitution with either  $-\text{XCH}_3$  groups or heteroaromatic groups, the electronic properties of the  $\text{Ru}^{\text{II}}$  complexes were well conserved (Supplementary Fig. 4, Table 1) suggesting that the  $\text{Ru}^{\text{II}}$  center is relatively well insulated from any electronic effects of substitution on the ligand. This was necessary to ensure that the only factors that would affect the rate of IET would be the hole delocalization in the oxidized photocatalyst and the degree of iodide-chalcogen interaction. A very different picture of the frontier molecular orbitals emerges for the one-electron oxidized  $\text{Ru}^{\text{III}}$  complexes. The bathochromic shifts of the emergent  $\text{Ru}^{\text{III}}$  absorption band suggest considerably more heteroatom involvement in the frontier orbitals of the  $\text{Ru}^{\text{III}}$  compounds, particularly the **X-Me** series, compared to the  $\text{Ru}^{\text{II}}$  compounds. Indeed, computational models generated of these compounds describe the new transition as a ligand-to-metal charge-transfer (LMCT) band with significant contributions from the heteroatom for the **X-Me** series, or from the aryl ring (but not the heteroatom) for the **X-Ar** series

(Supplementary Fig. 12, Supplementary Table 1). Furthermore, our DFT models of these Ru<sup>III</sup> complexes showed dramatic differences in the degree of delocalization of the frontier molecular orbitals (Supplementary Table 2). Of particular relevance to this study is the lowest unoccupied  $\beta$ -spin single electron molecular orbital ( $\beta$ -LUMO), which is equivalent to the positive hole of the oxidized catalyst. The degree of heteroatom contribution to this frontier orbital ( $c_{A,X}$ ) was determined using a Hirshfeld partitioning scheme (Table 2). In the **X-Me** series,  $c_{A,X}$  increased in the order O < S < Se, while in the **X-Ar** series, the heteroatoms contributed only nominally to the  $\beta$ -LUMO.

To investigate the relationship between  $c_{A,X}$  and IET, we have targeted the oxidation of iodide as a model reaction. The relevant energetically accessible one-electron oxidation process for iodide is expressed in equation 4<sup>68</sup>. The redox reaction with a photo-oxidized catalyst, Ox, ostensibly forms a short-lived adduct with one iodide ion prior to complete electron transfer with a second iodide ion (equation 5)<sup>69–71</sup>. Depending on the localization of the frontier molecular orbitals of Ox, it is conceivable that the [Ox...I...I]<sup>2-</sup> transition state would bring the acceptor orbitals of the catalyst into contact with the donor orbitals of one of the iodide ions. This would create a direct orbital pathway for electron transfer reminiscent of Taube's 1953 experiment. In contrast to Taube's model, however, no bridge is proposed in this study and the electron transfer occurs through the pathway created by direct overlap between of the iodide HOMO and the  $\beta$ -LUMO orbital of Ox.

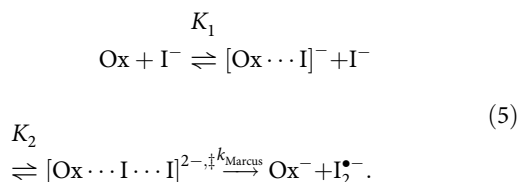
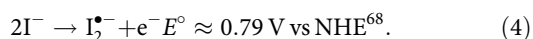
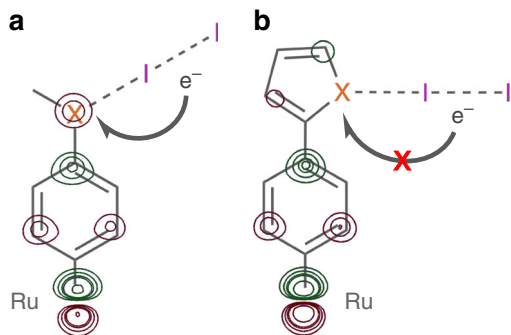


Figure 2c plots the log of  $k_{\text{IET}}$  as a function of  $c_{A,X}$ . A clear linear relationship is observed between the **X-Me** compounds that is not followed by the **X-Ar** series. These results suggest that there exists an orbital pathway for electron transfer through the chalcogen atoms of **X-Me** that does not exist for **X-Ar** (Fig. 4). In other words, iodide–chalcogen interactions in **X-Me** encourage overlap between the donor orbital of diiodide and the acceptor orbital of the oxidized catalyst, enabling fast IET. By contrast, the **X-Ar** series demonstrates that, in the absence of this orbital pathway, the iodide–chalcogen interaction is not capable of



**Fig. 4** Orbital pathway for IET. A schematic depicting the electron transfer pathway between diiodide **X-Me a** or **X-Ar b**, through the iodide–chalcogen interaction. The Ru complex fragment is overlaid with a contour plot of the  $\beta$ -LUMO down to an iso-value of 0.05

mediating IET. Whereas these results do not eliminate the possibility of other interactions mediating electron transfer in **X-Ar**, such as iodide interacting with the  $\pi$ -system of the thiophene or selenophene rings, the absence of any rate dependence on the identity of the chalcogen atom demonstrates that no orbital pathways exist through that atom.

If iodide–chalcogen interactions are indeed mediating an orbital interaction for IET, then it follows that the observed differences in  $k_{\text{IET}}$  among the **X-Me** series are predominantly a result of differences in  $H_{\text{DA}}$ . Unfortunately, the transient pre-ET [Ox...I...I]<sup>2-</sup> encounter complex could not be observed experimentally, nor could a stable geometry for this complex be found computationally, and therefore  $H_{\text{DA}}$  could not be evaluated directly. In order to investigate the dependence of  $k_{\text{IET}}$  on  $H_{\text{DA}}$ , the individual components that make up  $k_{\text{IET}}$  must be deconvoluted and evaluated separately. In practice, the observed second-order  $k_{\text{IET}}$  is related to the first-order electron transfer rate constant, as described by the Marcus equation ( $k_{\text{Marcus}}$ , equation 1), by an equilibrium constant,  $K_A$ , which represents the stepwise formation for the transient pre-ET [Ox...I...I]<sup>2-</sup> encounter complex (equation 6)<sup>72</sup>. As a result of this relationship, the observed trends in  $k_{\text{IET}}$  could result from differences either in  $K_A$ ,  $k_{\text{Marcus}}$ , or both.

$$k_{\text{IET}} = K_A k_{\text{Marcus}}. \quad (6)$$

The stepwise equilibrium constant  $K_A$  describes the formation of the [Ox...I...I]<sup>2-</sup> encounter complex. Due to the transient nature of this complex,  $K_A$  could not be quantified. As such, the effects of  $K_A$  on  $k_{\text{IET}}$  could only be evaluated approximately. In the absence of strongly electron-withdrawing groups bonded to the chalcogen, the interactions between iodide and soft atoms like sulfur and selenium are effectively van der Waals interactions and therefore expected to be too weak to draw iodide out of solution toward the oxidized catalyst. Furthermore, the rates of IET ( $10^3$ – $10^5 \text{ M}^{-1} \text{ s}^{-1}$ ) for our systems are low compared to the diffusion limit ( $\sim 10^{10} \text{ M}^{-1} \text{ s}^{-1}$ )<sup>73</sup>, and thus many transient catalyst...iodide interactions form and break within the lifetime of the oxidized complex. Stronger intermolecular interactions could therefore increase the lifetime of the initial [Ox...I] adduct, increasing the likelihood that a second iodide will encounter that adduct to create the [Ox...I...I]<sup>2-</sup> encounter complex and complete electron transfer. While this mechanism is plausible, it would predict the same rate enhancement for both **X-Ar** and **X-Me**, which is clearly not the case. Nonetheless, to eliminate this possibility, these adducts were modeled via DFT methods. The optimized interaction geometries are presented in Supplementary Figure 13 and the electronic energies of these interactions ( $\Delta E_{\text{int}}$ ) presented in Supplementary Table 3. These computational models show only a modest increase in adduct stability,  $K_1$ , between **O-Me** and the remaining compounds in the **X-Me** series, and actually predict a slight decrease in stability between **S-Me** and **Se-Me**. The initial [Ox...I] adduct stability clearly cannot account for the observed trends in  $k_{\text{IET}}$ . We have approximated the overall association constant  $K_A$  using semi-empirical methods (Supplementary Discussion, Supplementary Table 3), and found that, despite the differences in the association of the first iodide, the second iodide association,  $K_2$ , dominated the values for  $K_A$ . As a result,  $K_A$  was invariant with respect to compound identity. Because the calculations yielding these values for  $K_A$  are based on a number of rough approximations, we do not consider these values to be quantitatively accurate, however, given the homologous nature of the compounds under investigation in this study, any errors introduced by our assumptions should be consistent across both compound series, and therefore these  $K_A$  values are suitable to draw qualitative conclusions.

Because the observed trends in  $k_{\text{IET}}$  cannot be explained by the association constant  $K_{\text{A}}$ , it follows from equation 6 that these trends must arise from differences in  $k_{\text{Marcus}}$  instead. Following the Marcus equation (equation 1),  $k_{\text{Marcus}}$ —and by extension  $k_{\text{IET}}$ —primarily depends on the driving force for electron transfer,  $\Delta G^{\circ}_{\text{ET}}$ , the reorganization energy,  $\lambda$ , and the electronic coupling,  $H_{\text{DA}}$ . Of these,  $\Delta G^{\circ}_{\text{ET}}$  can be obtained from electrochemical measurements and  $\lambda$  can be estimated using relatively straightforward computational techniques, leaving  $H_{\text{DA}}$  as the only variable that cannot be directly evaluated. Among the compounds under investigation here,  $\lambda$  is unlikely to vary significantly as the compounds are structurally well conserved. This is supported by computational analysis which predict  $\lambda = \sim 1.33 \pm 0.03$  eV for all compounds under investigation (Supplementary Discussion, Supplementary Table 3). While the Ru<sup>III/II</sup> redox couples were relatively well conserved, the small differences that did exist will necessarily affect  $\Delta G^{\circ}_{\text{ET}}$  and in turn impact  $k_{\text{IET}}$  to some extent (Supplementary Discussion, Supplementary Table 3). That said, the trends in  $\Delta G^{\circ}_{\text{ET}}$  do not match the trends in  $k_{\text{IET}}$ , and therefore significant contributions from  $H_{\text{DA}}$  must be involved in our kinetic results. To better understand the importance of these contributions, and therefore better understand the relationship between  $k_{\text{IET}}$  and the heteroatom contributions to the  $\beta$ -LUMO,  $c_{\text{A,X}}$ , it is necessary to deconvolute the effects of  $\Delta G^{\circ}_{\text{ET}}$  and  $H_{\text{DA}}$  via a more involved analysis of our kinetic data.

Recently,  $H_{\text{DA}}$  has been shown to be roughly proportional to the overlap integral,  $S_{\text{DA}}$ , between the donor and acceptor frontier molecular orbitals,  $\phi_{\text{D}}$  and  $\phi_{\text{A}}$ , respectively (equation 7)<sup>38</sup>. In turn,  $\phi_{\text{A}}$  can be approximated as a linear combination of atomic orbitals,  $\varphi_{\text{A,i}}$ , from each atom  $i$  in the acceptor molecule, weighted by their individual contribution coefficients,  $c_{\text{A,i}}$  (equation 8). In the present study, we are concerned only with the iodide-heteroatom interaction, therefore for our purposes  $S_{\text{DA}}$  is approximated as the overlap between an empty p-orbital on the heteroatom,  $\varphi_{\text{A,X}}$ , weighted by  $c_{\text{A,X}}$  and a filled p-orbital on iodide,  $\varphi_{\text{D,I}}$  (equation 9). For simplicity, the donor is approximated as a single iodide, and therefore the corresponding contribution coefficient,  $c_{\text{D,I}}$ , is taken to be 1. The value  $S^{\circ}_{\text{DA}}$  is the overlap integral of a valence p-orbital of an isolated heteroatom cation and the 5p orbital of iodide, which can be calculated analytically using formulas developed by Mulliken (Supplementary Discussion, Supplementary Table 3)<sup>74</sup>. This approximate overlap integral  $c_{\text{A,X}}S^{\circ}_{\text{DA}}$  is unitless and directly proportional to  $H_{\text{DA}}$ , and therefore we can introduce a constant,  $A$ , with units of eV and a value of 1 to correct for units. Using this value  $Ac_{\text{A,X}}S^{\circ}_{\text{DA}}$  in place of  $H_{\text{DA}}$  in the Marcus equation allows us to generate a theoretical pseudo-rate constant, which we have denoted  $\gamma$  (Equation 10). This pseudo-rate constant differs from the true  $k_{\text{Marcus}}$  by a constant that is equivalent across all 5 compounds under investigation here.

$$H_{\text{DA}} \propto S_{\text{DA}} = \langle \phi_{\text{D}} | \phi_{\text{A}} \rangle. \quad (7)$$

$$\phi_{\text{A}} \approx \sum c_{\text{A,i}} \varphi_{\text{A,i}}. \quad (8)$$

$$S_{\text{DA}} \approx c_{\text{A,X}} \langle \varphi_{\text{D,I}} | \varphi_{\text{A,X}} \rangle = c_{\text{A,X}} S^{\circ}_{\text{DA}}. \quad (9)$$

$$\gamma = \frac{2\pi}{\hbar} |Ac_{\text{A,X}}S^{\circ}_{\text{DA}}|^2 \frac{1}{\sqrt{4\pi\lambda RT}} e^{\left(\frac{-(\lambda + \Delta G^{\circ}_{\text{ET}})^2}{4RT}\right)}. \quad (10)$$

Following equation 6,  $\gamma$  should also be proportional to  $k_{\text{IET}}$ , assuming a uniform association constant  $K_{\text{A}}$  across all compounds. We can therefore evaluate the relative importance of  $\Delta G^{\circ}_{\text{ET}}$ ,  $\lambda$ , and  $Ac_{\text{A,X}}S^{\circ}_{\text{DA}}$  (as a surrogate for  $H_{\text{DA}}$ ) by relating  $k_{\text{IET}}$

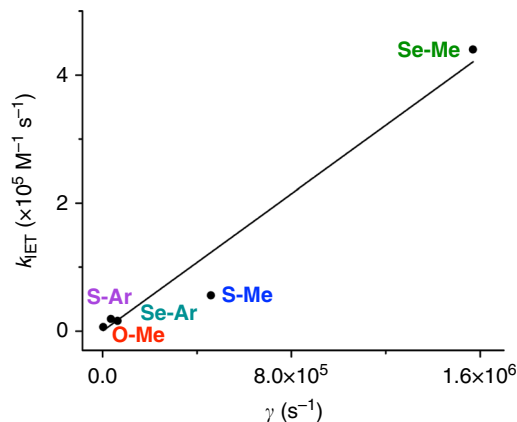


**Fig. 5** Relationship between  $k_{\text{IET}}$  and the pseudo-rate constant  $\gamma$  proportional to  $k_{\text{Marcus}}$ . A plot of  $k_{\text{IET}}$  for the indicated compounds as a function of the pseudo-rate-constant,  $\gamma$ , calculated analogously to  $k_{\text{Marcus}}$  but substituting  $Ac_{\text{A,X}}S^{\circ}_{\text{DA}}$  for  $H_{\text{DA}}$  (equation 10). The black line is a linear fit of the data with the  $x$  and  $y$  intercepts held at 0 (adj.  $R^2 = 0.968$ )

directly to  $\gamma$  (Fig. 5). Using  $\Delta G^{\circ}_{\text{ET}}$  values calculated from electrochemical data and  $\lambda$  values determined computationally (Supplementary Discussion, Supplementary Table 3), this plot reveals an approximately linear relationship between  $k_{\text{IET}}$  and  $\gamma$  for all 5 compounds under investigation. This analysis shows that our measured rate constants are consistent with Marcus theory and implies that, while not a perfect analogue,  $Ac_{\text{A,X}}S^{\circ}_{\text{DA}}$  provides a reasonable—and easily calculated—first approximation of the trends in  $H_{\text{DA}}$ . Additionally, this analysis can be used to illustrate the relative importance of  $\Delta G^{\circ}_{\text{ET}}$ ,  $\lambda$ , and  $Ac_{\text{A,X}}S^{\circ}_{\text{DA}}$  to the observed trends in  $k_{\text{IET}}$ . Supplemental Figure 14 shows how the linear relationship between  $k_{\text{IET}}$  and  $\gamma$  is affected when  $\gamma$  is recalculated using the average value of each of the critical variables. Ignoring the differences in  $Ac_{\text{A,X}}S^{\circ}_{\text{DA}}$  causes a complete loss in linearity (Supplementary Fig. 14a), while averaging  $\Delta G^{\circ}_{\text{ET}}$  or  $\lambda$  results in only minor deviations from linearity (Supplementary Fig. 14b,c). This result shows that  $Ac_{\text{A,X}}S^{\circ}_{\text{DA}}$ , and by extension  $H_{\text{DA}}$ , is the principal factor affecting  $k_{\text{IET}}$ . Finally, Supplemental Figures 14d and 14e show that if the differences in  $c_{\text{A,X}}$  are ignored then linearity is completely lost, while only a partial loss in linearity is observed if the differences in  $S^{\circ}_{\text{DA}}$  are ignored, thereby suggesting that  $c_{\text{A,X}}$  is the more important component of  $Ac_{\text{A,X}}S^{\circ}_{\text{DA}}$ .

Because,  $c_{\text{A,X}}$  and  $\lambda$  were both calculated using computational methods, there exists the possibility that these values, and by extension the conclusions we have drawn from Fig. 5, are sensitive to the DFT methodology used. To address this possibility, we have calculated  $c_{\text{A,X}}$  and  $\lambda$  using several popular DFT functionals (Supplementary Table 4). The absolute value of  $c_{\text{A,X}}$  varied somewhat between different functionals, particularly the pure generalized gradient functional BP86, however the trend among these values is well conserved in all cases.  $\lambda$  was largely invariant depending on the functional. Using these values, the linear relationship between  $k_{\text{IET}}$  and  $\gamma$  was found to be at least as strong, and in some cases stronger, with other functionals compared to PBE0 (Supplementary Figure 15). This result demonstrates that, while the choice of functional can have an effect of the quantitative results of our analysis, the qualitative conclusions are nonetheless supported under a wide variety of computational methods.

In conclusion, two parallel series of ruthenium-based catalysts have been synthesized bearing chalcogen-containing substituents in direct electronic contact with the ruthenium center. In the **X-Me** series, the  $\beta$ -LUMO of the oxidized compounds is

significantly delocalized onto the chalcogen atom, with increasing participation of that atom in the order  $O < S < Se$ . This increase in  $\beta$ -LUMO character on the heteroatom correlates with an increase in the electronic coupling term  $H_{DA}$  between the photo-oxidized catalyst and iodide, resulting in logarithmic increases in the observed rate of IET. The participation of the heteroatom in the  $\beta$ -LUMO is minimal for the X-Ar series and thus no change in  $k_{IET}$  is observed. These differences in  $k_{IET}$  clearly imply that iodide interacts with the chalcogen in oxidized X-Me<sup>•+</sup> to create an orbital pathway between iodide and the  $\beta$ -LUMO of the ruthenium complex, similar to the purported chloride bridge in Taube's 1953 experiment. This observation motivates the design of next-generation redox catalysts that enable orbital pathways for IET and suggests that simple, easily accessible DFT methods can serve as a predictive tool informing catalyst design.

## Methods

**Characterization of methyl esters in solution.** Acetonitrile was purchased from Sigma-Aldrich and purified on an MBraun solvent purification system prior to use. Tetrabutylammonium tetrafluoroborate was purchased from Alfa Aesar, recrystallized from boiling 50% water/ethanol, and dried under high vacuum prior to use. UV-visible spectra were recorded using ~30  $\mu$ M acetonitrile solutions on a Varian Cary 5000 spectrophotometer at a resolution of 1 nm. Cyclic voltammograms were recorded using a CH Instruments 660D potentiostat at room temperature using a standard three-electrode configuration (working electrode: 2 mm diameter Pt disc; reference electrode: RE-5B Ag/AgCl electrode in saturated aqueous potassium chloride (BASi Inc.), referenced externally to ferrocene/ferrocenium (0.630 V vs NHE);<sup>75</sup> counter electrode: Pt wire) in 0.1 M tetrabutylammonium tetrafluoroborate acetonitrile solutions.

**Characterization of functionalized thin films.** Acetonitrile was purchased from Honeywell (Burdick and Jackson, 99.99 %) and used as received. Sodium iodide (NaI, 99.9%), sodium perchlorate (NaClO<sub>4</sub>, >98%), and lithium perchlorate (LiClO<sub>4</sub>, 99.99%) were purchased from Sigma-Aldrich and used as received. UV-visible absorption spectra of the functionalized films were recorded on a Varian Cary 60 spectrophotometer with a resolution of 1 nm. Spectroelectrochemical measurements were performed using a WaveNow potentiostat (Pine Research Instrumentation, Inc.) at room temperature (22 ± 1 °C) with an AvaSpec-2048 fiber-optic spectrometer (Avantes) and an AvaLight-DHc light source (Avantes). Measurements used a standard three-electrode configuration (working electrode: functionalized nano-ITO on FTO; reference electrode: non-aqueous Ag/AgCl (0.5 M NaClO<sub>4</sub> in MeCN), referenced externally to ferrocene/ferrocenium (0.630 V vs NHE);<sup>75</sup> counter electrode: platinum wire) in 0.5 M NaClO<sub>4</sub>. The reference electrode was mounted in a Vycor-tipped glass tube with electrolyte to avoid contamination.

**General procedure for transient absorption experiments.** Transient absorption spectra and kinetics were acquired on an apparatus that has been described in literature<sup>76</sup>. Briefly, 532 nm excitation was achieved either with a frequency doubled Q-switched, pulsed Nd:YAG laser (Quantel USA (BigSky) Brilliant B; 532 nm, 5–6 ns full width at half-maximum (fwhm), 1 Hz, ~10 mm in diameter) or a laser of the same model, frequency tripled (355 nm) coupled to an optical parametric oscillator (OPO, Opotek, Inc.) tuned to 532 nm. The 532 nm beam was then directed through two Glan laser polarizers to attenuate the pulse fluence (typically kept between 0.5 and 1 mJ per pulse) and was directed 45° to the film surface. A 150 W xenon arc lamp (Applied Photophysics), pulsed with 70 V, served as the probe beam and was aligned orthogonally to the excitation laser. Before the sample, the light was focused through a monochromator (GM 252) to minimize background excitation of the samples. Detection was achieved with a monochromator (Spex 1702/04) optically coupled to an R928 photomultiplier tube (Hamamatsu). Transient data were acquired on a computer-interfaced digital oscilloscope (LeCroy 9450, Dual 350 MHz) with 2.5 ns resolution terminated at 50  $\Omega$ . For longer time-scale data acquisition, the xenon arc lamp was run continuously (not pulsed or shuttered) and the oscilloscope was terminated at 50 k $\Omega$ . To completely model the full kinetic decays data taken at multiple timescales were stitched together.

NaClO<sub>4</sub> and NaI electrolytes were prepared in acetonitrile and purged with argon for at least 15 min prior to use. The functionalized metal oxide thin films were placed in a 1 cm<sup>2</sup> cuvette with a 24/40 ground glass joint and fully submerged in argon-purged electrolyte solutions. The cuvette was then purged with argon for an additional 5 min and argon was continuously purged through the headspace of the cuvette throughout the measurements.

All single wavelength kinetic decays were modeled through the Kolrausch-Williams-Watts stretched exponential function<sup>77,78</sup>. The decay fitting was performed in Origin 2016pro, and least-squares error minimization was accomplished using the Levenberg-Marquardt iteration method.

**Full spectrum transient absorption.** Kinetic traces were monitored in 0.5 M LiClO<sub>4</sub>/MeCN from –10 to 90  $\mu$ s and collected every 10 nm between 400 and 800 nm. The laser power was ~2 mJ per pulse and 30 sequential laser pulses were averaged at each collected wavelength.

**IET and BET kinetics.** IET and BET kinetics were investigated using the functionalized SnO<sub>2</sub>-TiO<sub>2</sub> core-shell films submerged in fixed NaClO<sub>4</sub>/NaI acetonitrile solutions with a total salt concentration of 0.5 M. The ratio between the two was varied to monitor IET at varied iodide concentrations between 0 and 0.5 M. The laser power was attenuated to ensure the amount of oxidized dye produced upon excitation was low and similar between all compounds studied, between 0.5 and 1 mJ per pulse. Single wavelength kinetic decays were collected at 580 nm, close to an isosbestic point of the electric field effect for all compounds to ensure only IET was monitored. The final data were averaged between 90 and 150 laser pulses, to achieve an acceptable signal to noise ratio.

**Electrolyte recombination kinetics.** The kinetics of charge recombination between injected electrons and triiodide were monitored at 375 nm in 0.5 M NaI from –10  $\mu$ s to 1 s after pulsed laser excitation. The laser power was between 1 and 3 mJ per pulse. The final data were averaged over 500 laser pulses to achieve an acceptable signal to noise ratio.

**Additional methods.** Detailed descriptions of the synthetic procedures to prepare and characterize the X-Me and X-Ar compounds, the procedures to prepare functionalized metal oxide thin film samples, and the computational methods employed in this investigation can be found in Supplementary Methods section of Supplementary Information.

## Data availability

Supplementary Figures, Supplementary Methods, Supplementary Tables, and Supplementary Notes are included in the Supplementary Information file. DFT optimized molecular geometries and optical transitions calculated by time-dependent DFT are reported in the Supplementary Data 1 and Supplementary Data 2 files, respectively. Additional data supporting these findings are available from the corresponding authors upon request.

Received: 18 April 2018 Accepted: 18 October 2018

Published online: 21 November 2018

## References

- DuBois, D. L. Development of molecular electrocatalysts for energy storage. *Inorg. Chem.* **53**, 3935–3960 (2014).
- Alotto, P., Guarnieri, M. & Moro, F. Redox flow batteries for the storage of renewable energy: a review. *Renew. Sustain. Energy Rev.* **29**, 325–335 (2014).
- Yu, Z., Li, F. & Sun, L. Recent advances in dye-sensitized photoelectrochemical cells for solar hydrogen production based on molecular components. *Energy Environ. Sci.* **8**, 760–775 (2015).
- Tamaki, Y. & Ishitani, O. Supramolecular photocatalysts for the reduction of CO<sub>2</sub>. *ACS Catal.* **7**, 3394–3409 (2017).
- Grice, K. A. Carbon dioxide reduction with homogenous early transition metal complexes: opportunities and challenges for developing CO<sub>2</sub> catalysis. *Coord. Chem. Rev.* **336**, 78–95 (2017).
- Romero, N. A. & Nicewicz, D. A. Organic photoredox catalysis. *Chem. Rev.* **116**, 10075–10166 (2016).
- Skubi, K. L., Blum, T. R. & Yoon, T. P. Dual catalysis strategies in photochemical synthesis. *Chem. Rev.* **116**, 10035–10074 (2016).
- Nicewicz, D. A. & MacMillan, D. W. C. Merging photoredox catalysis with organocatalysis: the direct asymmetric alkylation of aldehydes. *Science* **322**, 77–80 (2008).
- Wehlin, S. A. M., Troian-Gautier, L., Li, G. & Meyer, G. J. Chloride oxidation by ruthenium excited-states in solution. *J. Am. Chem. Soc.* **139**, 12903–12906 (2017).
- Casarin, L., Swords, W. B., Caramori, S., Bignozzi, C. A. & Meyer, G. J. Rapid static sensitizer regeneration enabled by ion pairing. *Inorg. Chem.* **56**, 7324–7327 (2017).
- Young, E. R., Rosenthal, J., Hodgkiss, J. M. & Nocera, D. G. Comparative PCET study of a donor-acceptor pair linked by ionized and nonionized asymmetric hydrogen-bonded interfaces. *J. Am. Chem. Soc.* **131**, 7678–7684 (2009).
- Weinberg, D. R. et al. Proton-coupled electron transfer. *Chem. Rev.* **112**, 4016–4093 (2012).



13. Costentin, C., Robert, M. & Savéant, J.-M. Update 1 of electrochemical approach to the mechanistic study of proton-coupled electron transfer. *Chem. Rev.* **110**, PR1–PR40 (2010).
14. Robson, K. C. D., Hu, K., Meyer, G. J. & Berlinguette, C. P. Atomic level resolution of dye regeneration in the dye-sensitized solar cell. *J. Am. Chem. Soc.* **135**, 1961–1971 (2013).
15. Swords, W. B. et al. Evidence for interfacial halogen bonding. *Angew. Chem. Int. Ed. Engl.* **55**, 5956–5960 (2016).
16. Rosokha, S. V. Electron-transfer reactions of halogenated electrophiles: a different look into the nature of halogen bonding. *Faraday Discuss.* **203**, 315–332 (2017).
17. Rosokha, S. V. & Traversa, A. From charge transfer to electron transfer in halogen-bonded complexes of electrophilic bromocarbons with halide anions. *Phys. Chem. Chem. Phys.* **17**, 4989–4999 (2015).
18. Bietti, M., DiLabio, G. A., Lanzalunga, O. & Salamone, M. Time-resolved kinetic study of the electron-transfer reactions between ring-substituted cumyloxyl radicals and alkylferrocenes. Evidence for an inner-sphere mechanism. *J. Org. Chem.* **76**, 1789–1794 (2011).
19. Rosokha, S. V. & Kochi, J. K. Continuum of outer- and inner-sphere mechanisms for organic electron transfer. Steric modulation of the precursor complex in paramagnetic (ion-radical) self-exchanges. *J. Am. Chem. Soc.* **129**, 3683–3697 (2007).
20. Troian-Gautier, L., Beauvilliers, E. E., Swords, W. B. & Meyer, G. J. Redox active ion-paired excited states undergo dynamic electron transfer. *J. Am. Chem. Soc.* **138**, 16815–16826 (2016).
21. Kuss-Petermann, M. & Wenger, O. S. Increasing electron-transfer rates with increasing donor-acceptor distance. *Angew. Chem. Int. Ed. Engl.* **55**, 815–819 (2016).
22. Grampp, G. The Marcus inverted region from theory to experiment. *Angew. Chem. Int. Ed. Engl.* **32**, 691–693 (1993).
23. Marcus, R. A. Chemical and electrochemical electron-transfer theory. *Annu. Rev. Phys. Chem.* **15**, 155–196 (1964).
24. Sutin, N. Theory of electron transfer reactions: insights and hindsight. In *Progress in Inorganic Chemistry* (ed. Lippard, S. J.) **30**, 441–498 (John Wiley & Sons Inc., New York, 1983).
25. Sutin, N. Nuclear, electronic, and frequency factors in electron transfer reactions. *Acc. Chem. Res.* **15**, 275–282 (1982).
26. Sutin, N. Comparison of observed and calculated parameters for electron exchange: electron-transfer and electrochemical reactions; photochemical and other energized reactions. In *Inorganic Reactions and Methods* (eds. Zuckerman, J. J. & Hagen, A. P.) **15**, 32–37 (VCH Publishers Inc., Deerfield Beach, 1986).
27. Creutz, C. & Sutin, N. Electronic factors: nonadiabaticity: electron-transfer and electrochemical reactions; photochemical and other energized reactions. In *Inorganic Reactions and Methods* (eds. Zuckerman, J. J. & Hagen, A. P.) **15**, 58–59 (VCH Publishers Inc., Deerfield Beach, 1986).
28. Chan, M.-S. & Wahl, A. C. Rate of electron exchange between iron, ruthenium, and osmium complexes containing 1,10-phenanthroline, 2,2'-bipyridyl, or their derivatives from nuclear magnetic resonance studies. *J. Phys. Chem.* **82**, 2542–2549 (1978).
29. Rotzinger, F. P. Structure and properties of the precursor/successor complex and transition state of the  $\text{CrCl}_2^{2+}/\text{Cr}^{2+}$  electron self-exchange reaction via the inner-sphere pathway. *Inorg. Chem.* **53**, 9923–9931 (2014).
30. Hsu, C.-P. The electronic couplings in electron transfer and excitation energy transfer. *Acc. Chem. Res.* **42**, 509–518 (2009).
31. Parthey, M. & Kaupp, M. Quantum-chemical insights into mixed-valence systems: within and beyond the Robin–Day scheme. *Chem. Soc. Rev.* **43**, 5067–5088 (2014).
32. Omberg, K. M., Chen, P. & Meyer, T. J. Spectroscopic determination of electron transfer barriers and rate constants. In *Advances in Chemical Physics: Electron Transfer—from Isolated Molecules to Biomolecules* (eds. Jortner, J., Bixon, M., Prigogne, I. & Rice, S. A.) **106**, 553–570 (John Wiley & Sons, Inc., New York, 1999).
33. Hush, N. S. Distance dependence of electron transfer rates. *Coord. Chem. Rev.* **64**, 135–157 (1985).
34. Cave, R. J. & Newton, M. D. Generalization of the Mulliken-Hush treatment for the calculation of electron transfer matrix elements. *Chem. Phys. Lett.* **249**, 15–19 (1996).
35. Heckmann, A. & Lambert, C. Organic mixed-valence compounds: a playground for electrons and holes. *Angew. Chem. Int. Ed. Engl.* **51**, 326–392 (2012).
36. Brunschwig, B. Y. B. S., Creutz, C. & Macartney, D. H. The role of inner-sphere configuration changes in electron-exchange reactions of metal complexes. *Faraday Discuss. Chem. Soc.* **74**, 113–127 (1982).
37. Kubas, A. et al. Electronic couplings for molecular charge transfer: benchmarking CDFI, FODFI, and FODFTB against high-level ab initio calculations. *J. Chem. Phys.* **140**, 104105–104122 (2014).
38. Gajdos, F. et al. Ultrafast estimation of electronic couplings for electron transfer between  $\pi$ -conjugated organic molecules. *J. Chem. Theory Comput.* **10**, 4653–4660 (2014).
39. Taube, H., Myers, H. & Rich, R. L. Observations on the mechanism of electron transfer in solution. *J. Am. Chem. Soc.* **75**, 4118–4119 (1953).
40. Haim, A. Role of the bridging ligand in inner-sphere electron-transfer reactions. *Acc. Chem. Res.* **8**, 264–272 (1975).
41. Richardson, D. E. & Taube, H. Mixed-valence molecules: electronic delocalization and stabilization. *Coord. Chem. Rev.* **60**, 107–129 (1984).
42. Chou, M. H., Creutz, C. & Sutin, N. Donor-acceptor electronic coupling as a function of bridging group: mixed-valence diruthenium(II,III) complexes bridged by isonicotinato and isonicotinamido ligands. *Inorg. Chem.* **31**, 2318–2327 (1992).
43. Richardson, D. E. & Taube, H. Electronic interactions in mixed-valence molecules as mediated by organic bridging groups. *J. Am. Chem. Soc.* **105**, 40–51 (1983).
44. Creutz, C., Newton, M. D. & Sutin, N. Metal-ligand and metal-metal coupling elements. *J. Photochem. Photobiol. A Chem.* **82**, 47–59 (1994).
45. Beratan, D. N., Betts, J. N. & Onuchic, J. N. Protein electron transfer rates set by the bridging secondary and tertiary structure. *Science* **252**, 1285–1288 (1991).
46. Lin, J., Balabin, I. A. & Beratan, D. N. The nature of aqueous tunneling pathways between electron-transfer proteins. *Science* **310**, 1311–1313 (2005).
47. Onuchic, J. N., Beratan, D. N., Winkler, J. R. & Gray, H. B. Pathway analysis of protein electron-transfer reactions. *Annu. Rev. Biophys. Biomol. Struct.* **21**, 349–377 (1992).
48. de Rege, P. J., Williams, S. A. & Therien, M. J. Direct evaluation of electronic coupling mediated by hydrogen bonds: implications for biological electron transfer. *Science* **269**, 1409–1413 (1995).
49. Kumar, K., Lin, Z., Waldeck, D. H. & Zimmt, M. B. Electronic coupling in C-clamp-shaped molecules: solvent-mediated superexchange pathways. *J. Am. Chem. Soc.* **118**, 243–244 (1996).
50. Read, I., Napper, A., Kaplan, R., Zimmt, M. B. & Waldeck, D. H. Solvent-mediated electronic coupling: the role of solvent placement. *J. Am. Chem. Soc.* **121**, 10976–10986 (1999).
51. Kaplan, R., Napper, A. M., Waldeck, D. H. & Zimmt, M. B. The role played by orbital energetics in solvent mediated electronic coupling. *J. Phys. Chem. A* **106**, 1917–1925 (2002).
52. Kang, Y. K., Iovine, P. M. & Therien, M. J. Electron transfer reactions of rigid, cofacially compressed,  $\pi$ -stacked porphyrin-bridge-quinone systems. *Coord. Chem. Rev.* **255**, 804–824 (2011).
53. Sakamaki, D. et al. 1,3,5-Benzenetriamine double- and triple-decker molecules. *Angew. Chem. Int. Ed. Engl.* **51**, 8281–8285 (2012).
54. Yokoyama, Y., Sakamaki, D., Ito, A., Tanaka, K. & Shiro, M. A triphenylamine double-decker: from a delocalized radical cation to a diradical dication with an excited triplet state. *Angew. Chem. Int. Ed. Engl.* **51**, 9403–9406 (2012).
55. Skourtis, S. S. & Beratan, D. N. Theories of structure–function relationships for bridge-mediated electron transfer reactions. In *Advances in Chemical Physics: Electron Transfer—from Isolated Molecules to Biomolecules* (eds. Jortner, J., Bixon, M., Prigogne, I. & Rice, S. A.) **106**, 377–452 (John Wiley & Sons, Inc., New York, 1999).
56. Natali, M., Campagna, S. & Scandola, F. Photoinduced electron transfer across molecular bridges: electron- and hole-transfer superexchange pathways. *Chem. Soc. Rev.* **43**, 4005–4018 (2014).
57. Kirkpatrick, J. An approximate method for calculating transfer integrals based on the ZINDO Hamiltonian. *Int. J. Quantum Chem.* **108**, 51–56 (2008).
58. Oberhofer, H. & Blumberger, J. Revisiting electronic couplings and incoherent hopping models for electron transport in crystalline C60 at ambient temperatures. *Phys. Chem. Chem. Phys.* **14**, 13846–13852 (2012).
59. Mukherjee, A. J., Zade, S. S., Singh, H. B. & Sunoj, R. B. Organoselenium chemistry: role of intramolecular interactions. *Chem. Rev.* **110**, 4357–4416 (2010).
60. Lim, J. Y. C. et al. Chalcogen bonding macrocycles and [2]rotaxanes for anion recognition. *J. Am. Chem. Soc.* **139**, 3122–3133 (2017).
61. Garrett, G. E., Gibson, G. L., Straus, R. N., Seferos, D. S. & Taylor, M. S. Chalcogen bonding in solution: interactions of benzotelluradiazoles with anionic and uncharged Lewis bases. *J. Am. Chem. Soc.* **137**, 4126–4133 (2015).
62. Hu, K. et al. Direct spectroscopic evidence for constituent heteroatoms enhancing charge recombination at a  $\text{TiO}_2$ –ruthenium dye interface. *J. Phys. Chem. C* **118**, 17079–17089 (2014).
63. O'Regan, B. C. et al. Structure/function relationships in dyes for solar energy conversion: a two-atom change in dye structure and the mechanism for its effect on cell voltage. *J. Am. Chem. Soc.* **131**, 3541–3548 (2009).
64. Aghazada, S. et al. Unraveling the dual character of sulfur atoms on sensitizers in dye-sensitized solar cells. *ACS Appl. Mater. Interfaces* **8**, 26827–26833 (2016).

65. Wee, K.-R. et al. An aqueous, organic dye derivatized SnO<sub>2</sub>/TiO<sub>2</sub> core/shell photoanode. *J. Mater. Chem. A Mater. Energy Sustain* **4**, 2969–2975 (2016).
66. Bomben, P. G., Robson, K. C. D., Sedach, P. A. & Berlinguette, C. P. On the viability of cyclometalated Ru(II) complexes for light-harvesting applications. *Inorg. Chem.* **48**, 9631–9643 (2009).
67. Bomben, P. G., Robson, K. C. D., Koivisto, B. D. & Berlinguette, C. P. Cyclometalated ruthenium chromophores for the dye-sensitized solar cell. *Coord. Chem. Rev.* **256**, 1438–1450 (2012).
68. Boschloo, G., Gibson, E. A. & Hagfeldt, A. Photomodulated voltammetry of iodide/triiodide redox electrolytes and its relevance to dye-sensitized solar cells. *J. Phys. Chem. Lett.* **2**, 3016–3020 (2011).
69. Boschloo, G. & Hagfeldt, A. Characteristics of the iodide/triiodide redox mediator in dye-sensitized solar cells. *Acc. Chem. Res.* **42**, 1819–1826 (2009).
70. Anderson, A. Y., Barnes, P. R. F., Durrant, J. R. & O'Regan, B. C. Quantifying regeneration in dye-sensitized solar cells. *J. Phys. Chem. C* **115**, 2439–2447 (2011).
71. Privalov, T., Boschloo, G., Hagfeldt, A., Svensson, P. H. & Kloo, L. A study of the interactions between I<sup>-</sup>/I<sub>3</sub><sup>-</sup> redox mediators and organometallic sensitizing dyes in solar cells. *J. Phys. Chem. C* **113**, 783–790 (2009).
72. Marcus, R. A. & Sutin, N. Electron transfers in chemistry and biology. *Biochim. Et. Biophys. Acta (BBA) - Rev. Bioenerg.* **811**, 265–322 (1985).
73. Rowley, J. G., Farnum, B. H., Ardo, S. & Meyer, G. J. Iodide chemistry in dye-sensitized solar cells: making and breaking I–I bonds for solar energy conversion. *J. Phys. Chem. Lett.* **1**, 3132–3140 (2010).
74. Mulliken, R. S., Rieke, C. A., Orloff, D. & Orloff, H. Formulas and numerical tables for overlap integrals. *J. Chem. Phys.* **17**, 1248–1267 (1949).
75. Pavlishchuk, V. V. & Addison, A. W. Conversion constants for redox potentials measured versus different reference electrodes in acetonitrile solutions at 25 °C. *Inorg. Chim. Acta* **298**, 97–102 (2000).
76. Argazzi, R., Bignozzi, C. A., Heimer, T. A., Castellano, F. N. & Meyer, G. J. Enhanced spectral sensitivity from ruthenium(II) polypyridyl based photovoltaic devices. *Inorg. Chem.* **33**, 5741–5749 (1994).
77. Williams, G. & Watts, D. C. Non-symmetrical dielectric relaxation behaviour arising from a simple empirical decay function. *Trans. Faraday Soc.* **66**, 80–85 (1970).
78. Lindsey, C. P. & Patterson, G. D. Detailed comparison of the Williams–Watts and Cole–Davidson functions. *J. Chem. Phys.* **73**, 3348–3357 (1980).

## Acknowledgements

The authors would like to thank Dr. Degao Wang and Dr. Thomas Meyer at the University of North Carolina at Chapel Hill for their assistance in preparing the SnO<sub>2</sub>/TiO<sub>2</sub> core-shell thin films used in this study. The University of British Columbia authors are grateful to the Canadian Natural Science and Engineering Research Council (RGPIN 337345-13), Canadian Foundation for Innovation (229288), Canadian Institute for Advanced Research (BSE-BERL-162173), and Canada Research Chairs for financial

support. University of North Carolina at Chapel Hill authors acknowledge support from the Division of Chemical Sciences, Office of Basic Energy Sciences, Office of Energy Research, U.S. Department of Energy (Grant DE-SC0013461). W.B.S. and M.D.T. acknowledge the support from the National Science Foundation Graduate Research Fellowship Program (Grant DGE-1650116). This work made use of atomic layer deposition instrumentation at the Chapel Hill Analytical and Nanofabrication Laboratory (CHANL), a member of the North Carolina Research Triangle Nanotechnology Network (RTNN), which is supported by the National Science Foundation (Grant ECCS-1542015) as part of the National Nanotechnology Coordinated Infrastructure (NNCI).

## Author contributions

C.W.K. and C.P.B. designed the experiment. C.W.K. prepared the compounds, performed the solution-phase characterization, and performed the computational analysis. W.B.S., M.D.T., and G.J.M. performed the surface-anchored characterization and the kinetic experiments. C.W.K. and C.P.B. wrote the manuscript and all authors contributed to discussing and editing the content.

## Additional information

**Supplementary Information** accompanies this paper at <https://doi.org/10.1038/s41467-018-07263-1>.

**Competing interests:** The authors declare no competing interests.

**Reprints and permission** information is available online at <http://npg.nature.com/reprintsandpermissions/>

**Publisher's note:** Springer Nature remains neutral with regard to jurisdictional claims in published maps and institutional affiliations.



**Open Access** This article is licensed under a Creative Commons Attribution 4.0 International License, which permits use, sharing, adaptation, distribution and reproduction in any medium or format, as long as you give appropriate credit to the original author(s) and the source, provide a link to the Creative Commons license, and indicate if changes were made. The images or other third party material in this article are included in the article's Creative Commons license, unless indicated otherwise in a credit line to the material. If material is not included in the article's Creative Commons license and your intended use is not permitted by statutory regulation or exceeds the permitted use, you will need to obtain permission directly from the copyright holder. To view a copy of this license, visit <http://creativecommons.org/licenses/by/4.0/>.

© The Author(s) 2018